



# Au- $\text{ZnFe}_2\text{O}_4$ hollow microspheres based gas sensor for detecting the mustard gas simulant 2-chloroethyl ethyl sulfide

Junchao Yang<sup>1</sup> · Molin Qin<sup>1</sup> · Yong Pan<sup>1</sup> · Liu Yang<sup>1</sup> · Jianan Wei<sup>1</sup> · CanCan Yan<sup>1</sup> · Genwei Zhang<sup>1</sup> · Shuya Cao<sup>1</sup> · Qibin Huang<sup>1</sup>

Received: 4 March 2024 / Accepted: 2 April 2024  
© The Author(s) 2024

## Abstract

Mustard gas, a representative of blister agents, poses a severe threat to human health. Although the structure of 2-chloroethyl ethyl sulfide (2-CEES) is similar to mustard gas, 2-CEES is non-toxic, rendering it a commonly employed simulant in related research.  $\text{ZnFe}_2\text{O}_4$ -based semiconductor gas sensors exhibit numerous advantages, including structural stability, high sensitivities, and easy miniaturization. However, they exhibit insufficient sensitivity at low concentrations and require high operating temperatures. Owing to the effect of electronic and chemical sensitization, the gas-sensing performance of a sensor may be remarkably enhanced via the sensitization method of noble metal loading. In this study, based on the morphologies of  $\text{ZnFe}_2\text{O}_4$  hollow microspheres, a solvothermal method was adopted to realize different levels of Au loading. Toward 1 ppm of 2-CEES, the gas sensor based on 2 wt.% Au-loaded  $\text{ZnFe}_2\text{O}_4$  hollow microspheres exhibited a response sensitivity twice that of the gas sensor based on pure  $\text{ZnFe}_2\text{O}_4$ ; furthermore, the response/recovery times decreased. Additionally, the sensor displayed excellent linear response to low concentrations of 2-CEES, outstanding selectivity in the presence of several common volatile organic compounds, and good repeatability, as well as long-term stability. The Au-loaded  $\text{ZnFe}_2\text{O}_4$ -based sensor has considerable potential for use in detecting toxic chemical agents and their simulants.

**Keywords** 2-CEES · Au loading · Chemical warfare agent · Gas sensor ·  $\text{ZnFe}_2\text{O}_4$

## Introduction

Mustard gas, as a representative toxic chemical vesicant, has been extensively used in chemical warfare. It is the most produced and stored chemical weapon to date, causing significant casualties and posing a grave threat to human health and societal stability. Mustard gas is also regarded as the “king of the toxins,” [1–4] and exhibits high toxicity, with an “immediately dangerous to life or health” concentration of 0.1 ppm [5]. Notably, no antidotes for mustard gas have been reported thus far, and only symptomatic treatments can be administered. Therefore, the rapid, accurate detection and

identification of mustard gas are critical [6, 7]. The non-toxic simulant 2-chloroethyl ethyl sulfide (2-CEES) has a chemical structure similar to that of mustard gas; therefore, it is commonly used in related research [8–10].

Currently, the primary methods of detecting toxic chemical agents and their simulants include laser [11], infrared [12], Raman [13], and ion mobility spectroscopies [14], mass spectrometry [15], surface acoustic wave sensing [16], and gas sensing using metal oxide semiconductors [17–19]. Owing to their simplicity, low costs, and ease of miniaturization [20–22], metal oxide semiconductor sensors have received considerable attention, and have been employed in detecting toxic gases at low concentrations. In addition, sensing materials, such as  $\text{WO}_3$  [23],  $\text{ZnO}$  [24],  $\text{CdSnO}_3$  [25], and  $\text{Fe}_2\text{O}_3$  [26], have been applied in detecting the mustard gas simulant 2-CEES.

The binary metal oxide  $\text{ZnFe}_2\text{O}_4$  is characterized by a narrow bandgap (2.1 eV), structural stability, and abundant oxygen vacancies. It has recently attracted attention in the field of gas sensing [27–31]. In a previous study [17], a  $\text{ZnFe}_2\text{O}_4$  microsphere-based gas sensor was designed for

✉ Junchao Yang  
yangjunchao1990@163.com

✉ Shuya Cao  
13910919731@139.com

✉ Qibin Huang  
huangqibin@sklnbc.com

<sup>1</sup> State Key Laboratory of NBC Protection for Civilian, Beijing 100000, China

detecting 2-CEES; however, challenges such as high operating temperatures, inadequate sensitivity at low concentrations, and prolonged response/recovery times still need to be addressed. Numerous studies have reported that the gas-sensing performance of metal oxide sensors can be significantly enhanced through noble metal loading [32–35], heterogeneous ion doping [36–38], and heterojunction formation [39–41]. Notably, noble metals with catalytic properties, such as Au, Ag, Pt, and Pd, may enhance the reaction efficiencies of target gas molecules on the surfaces of semiconductor metal oxides and reduce the activation energy required for the reaction. Accordingly, the sensitivities of gas sensors and their response/recovery rates may be improved while reducing their levels of energy consumption. This mechanism of sensitivity enhancement is known as the effect of chemical and electronic sensitization caused by noble metals [42–47]. As an example, Kim et al. prepared a 0.6 wt.% Pd-loaded ZnO nanofiber-based gas sensor with a sensitivity of 74.7 toward 100 ppb H<sub>2</sub> at a working temperature of 350 °C [48]. Patil et al. fabricated a Pt-CdSnO<sub>3</sub> thin-film sensor, and compared to the pure CdSnO<sub>3</sub> thin film, it exhibited a superior response sensitivity toward 2-CEES as well as enhanced response and recovery times [49].

In this study, Au-loaded ZnFe<sub>2</sub>O<sub>4</sub> hollow microspheres were prepared using a solvothermal method and used to fabricate gas sensors. Gas sensitivity studies were performed using the mustard gas simulant 2-CEES, and the enhanced sensing mechanism was revealed via microstructural characterization.

## Material and methods

### Materials and reagents

The chemicals used in this study, including Zn(NO<sub>3</sub>)<sub>2</sub>·6H<sub>2</sub>O, Fe(NO<sub>3</sub>)<sub>3</sub>·9H<sub>2</sub>O, urea, glycerol, isopropanol, ethanol, HAuCl<sub>4</sub>·4H<sub>2</sub>O, and sodium citrate dihydrate (with a relative molar mass of 258.07 g/mol), were obtained from Sinopharm (Beijing, China). The reagents were of analytical grade and used without further purification.

### Synthesis and preparation of the materials

Firstly, 0.252 g of HAuCl<sub>4</sub>·4H<sub>2</sub>O and 0.237 g of sodium citrate dihydrate were separately dissolved in deionized H<sub>2</sub>O in 10 mL volumetric flasks, and the solutions were then diluted to the mark.

Secondly, Zn(NO<sub>3</sub>)<sub>2</sub>·6H<sub>2</sub>O (0.5 mmol, 0.149 g), Fe(NO<sub>3</sub>)<sub>3</sub>·9H<sub>2</sub>O (1.0 mmol, 0.404 g), and urea (1 mmol, 0.060 g) were added to the sodium citrate solution, along with 0, 100, 200, 300, or 400 μL of the HAuCl<sub>4</sub> solution. The resulting solution was added to a mixture of glycerol

and isopropanol (4 and 16 mL, respectively), which was then stirred for 30 min. The solution was transferred to a 50 mL reaction vessel, and the hydrothermal reaction was allowed to proceed at 180 °C for 24 h. Subsequently, the solution was centrifuged in deionized H<sub>2</sub>O and then ethanol at 9000 rpm for 8 min, with the centrifugation protocol repeated three times. The solution was then dried in a vacuum oven at 80 °C for 12 h, and finally, the dried sample was calcined in a muffle furnace at 450 °C, with a heating rate of 2 °C/min, for 2 h. Thus, ZnFe<sub>2</sub>O<sub>4</sub> samples loaded with 0, 1, 2, 3, or 4 wt.% Au were obtained.

### Characterization of the sensing materials

The structural morphology was observed using scanning electron microscopy (SEM, Gemini 300, ZEISS, Oberkochen, Germany) and transmission electron microscopy (TEM, JEM-F200, JEOL, Tokyo, Japan). The crystalline phases were determined via X-ray diffraction (XRD, Empyrean, Malvern Panalytical, Malvern, UK) with a Cu target and K $\alpha$ 1 radiation ( $\lambda = 0.154056$  nm). The elemental compositions were analyzed using energy-dispersive X-ray spectroscopy (EDS, JED-2300T, JEOL). The chemical compositions were determined using X-ray photoelectron spectroscopy (XPS, K-Alpha, Thermo Fisher Scientific, Waltham, MA, USA) at a working voltage and filament current of 12 V and 6 mA, respectively. The working voltage and filament current of 12 V and 6 mA, respectively. The electron binding energies were calibrated using the C 1s peak (284.8 eV).

### Fabrication and evaluation of the gas-sensing device

The gas sensor was fabricated as follows. First, the as-prepared ZnFe<sub>2</sub>O<sub>4</sub> sample was added to a suitable amount of deionized water H<sub>2</sub>O to form a uniform slurry. The slurry was evenly coated onto ceramic Al<sub>2</sub>O<sub>3</sub> tubes (with Au electrodes at both ends and Pt wires as leads for the testing electrodes) using a fine brush to form thin films. After drying in the air, the samples were sintered at 300 °C for 2 h. Subsequently, a Ni–Cr alloy heating wire was placed inside the ceramic tube and welded to a six-legged base; the procedure is shown in Fig. 1a, b.

The gas sensor was evaluated as follows. First, the as-prepared gas-sensing device was aged for  $\geq 72$  h using an aging platform. The device was then placed in an eight-channel testing chamber (Fig. 2e), and the chemical toxicants or simulants were placed as shown in Fig. 2c. The concentration of the target gas could be adjusted by controlling the temperature and gas flow rate in the generation chamber using a controller (Fig. 2b). The working temperature of the device could be adjusted by controlling the temperature of

**Fig. 1** Schematic of the gas-sensing device: **a** Structure of the side-heated sensor and **b** image of the real product [17]

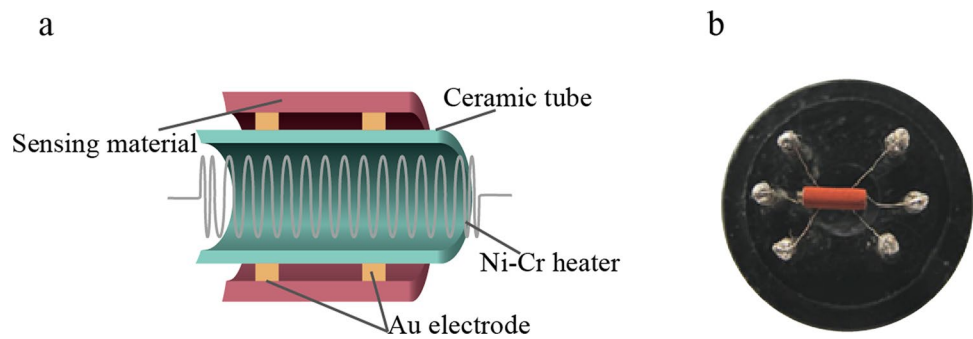
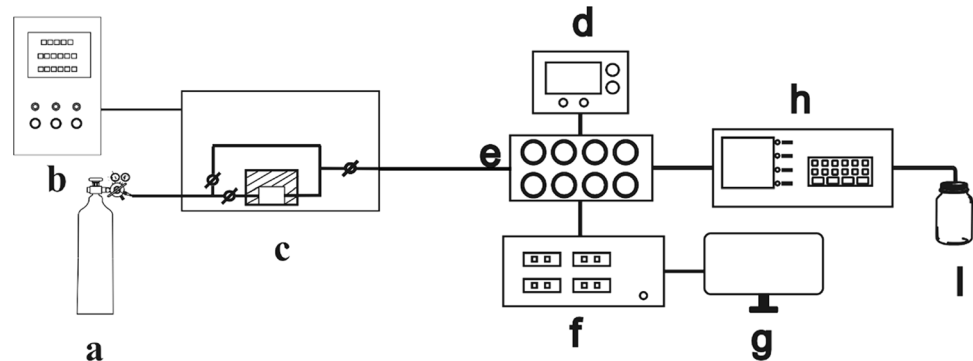


**Fig. 2** Dynamic testing platform: **a** Gas cylinder; **b** Generation system controller; **c** Dynamic generation system; **d** Direct-current potential regulator; **e** Eight-channel testing chamber; **f** Test source table; **g** Workstation; **h** Concentration monitor; **i** Exhaust cylinder [17]



the heating wire using a power source (Fig. 2d). The real-time concentration data of the generation chamber were detected using a monitor (Fig. 2h). The real-time resistance data shown in Fig. 2f could be obtained using the workstation shown in Fig. 2g for further data processing.

The sensitivity of the sensor is defined as  $S = R_a/R_g$ , where  $R_a$  and  $R_g$  are the respective resistances of the device in air and the stable state under the testing gas. The response ( $t_{res}$ ) and recovery times ( $t_{rec}$ ) of the device are defined as the times required for the gas-sensitive component to reach 90% of the total changes in resistance during adsorption and desorption.

## Results and discussion

### Structure and morphology

Figure 3 shows the XRD patterns of the as-prepared Au-loaded ZnFe<sub>2</sub>O<sub>4</sub> samples. The diffraction peaks of the samples with five different Au loading ratios at  $2\theta = 29.92^\circ$ ,  $35.24^\circ$ ,  $56.61^\circ$ , and  $62.16^\circ$  are attributed to the (220), (311), (333), and (440) crystal planes of ZnFe<sub>2</sub>O<sub>4</sub>, respectively, based on the standard diffraction pattern (JCPDS: 82–1049) [29]. Conversely, the diffraction peaks at  $2\theta = 38.18^\circ$ ,  $44.37^\circ$ ,  $64.56^\circ$ , and  $77.54^\circ$  may be attributed to the (100), (200), (220), and (311) crystal planes of Au, respectively, according to the standard diffraction pattern (JCPDS:

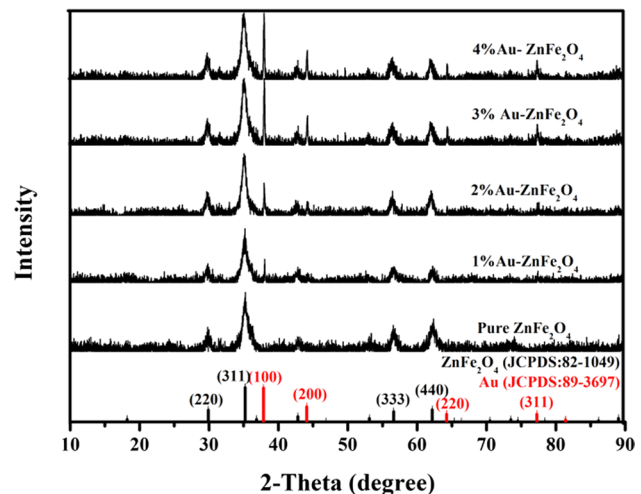


**Fig. 3** XRD patterns of the Au-loaded ZnFe<sub>2</sub>O<sub>4</sub> samples with different Au loading ratios

89–3697) [34]. Moreover, the intensities of the Au diffraction peaks increase with increasing Au loading. Notably, no peaks representing impurities or other crystalline phases are observed in the XRD patterns. Therefore, the five as-synthesized samples, including pure ZnFe<sub>2</sub>O<sub>4</sub> and ZnFe<sub>2</sub>O<sub>4</sub> loaded with small amounts of Au, exhibit high purities and no other heterogeneous phases.

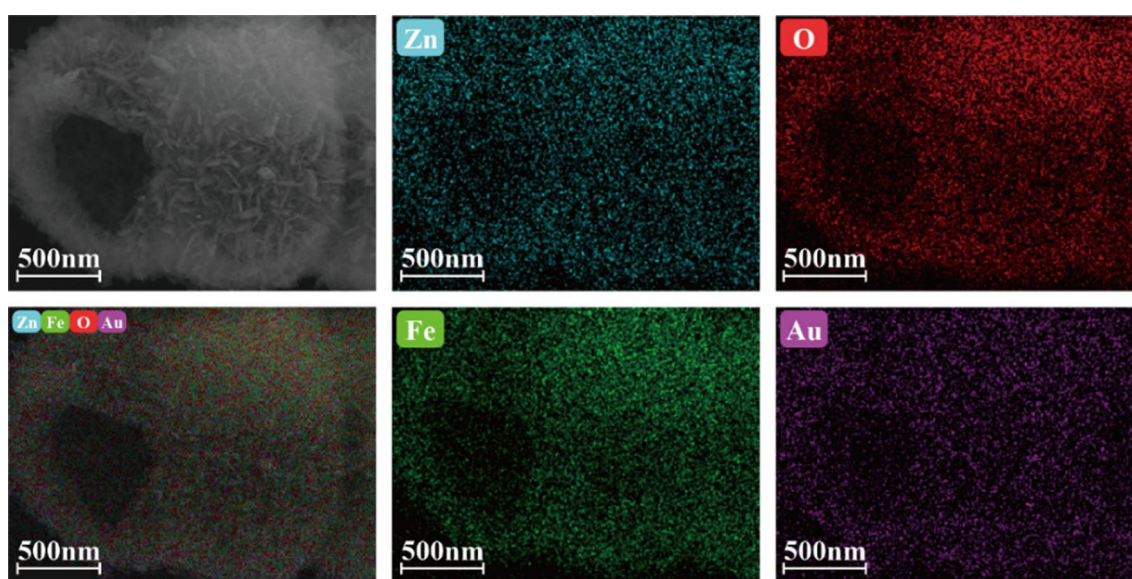
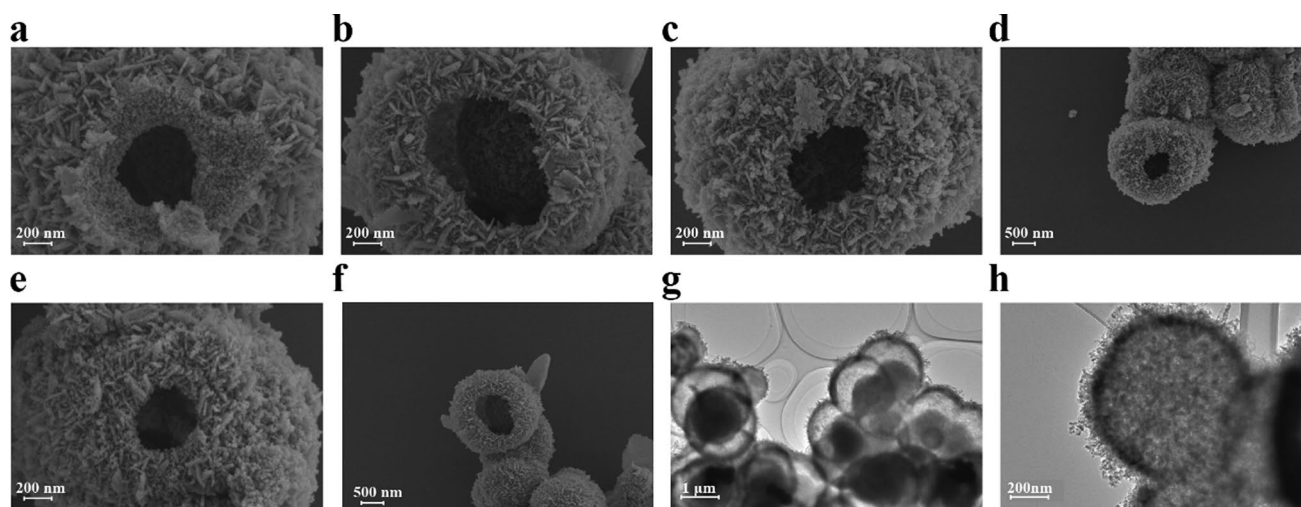
EDS of the as-prepared ZnFe<sub>2</sub>O<sub>4</sub> samples was performed, and the corresponding mass fractions of each element are

**Table 1** Mass fractions of the elements in the Au-loaded ZnFe<sub>2</sub>O<sub>4</sub> samples with different Au loading ratios

Material	Fe (%)	Zn (%)	O (%)	Au (%)
Pure-ZnFe <sub>2</sub> O <sub>4</sub>	45.67	26.41	27.92	0
1 wt% Au—ZnFe <sub>2</sub> O <sub>4</sub>	46.82	25.73	26.58	0.87
2 wt% Au—ZnFe <sub>2</sub> O <sub>4</sub>	43.65	24.81	29.41	2.13
3 wt% Au—ZnFe <sub>2</sub> O <sub>4</sub>	44.86	25.27	27.01	2.86
4 wt% Au—ZnFe <sub>2</sub> O <sub>4</sub>	45.24	23.93	26.61	4.22

listed in Table 1. The mass fractions of Au in these five samples are 0, 0.87, 2.13, 2.86, and 4.22%, which are close to the theoretical values. Therefore, the method of loading Au onto the ZnFe<sub>2</sub>O<sub>4</sub> samples is viable. Based on the EDS results for 2 wt.% Au-ZnFe<sub>2</sub>O<sub>4</sub> (Fig. 4), the presence of Zn, Fe, O, and Au in the sample and their uniform distributions within the ZnFe<sub>2</sub>O<sub>4</sub> hollow microspheres are consistent with the XRD results.

According to the SEM images of the ZnFe<sub>2</sub>O<sub>4</sub> samples loaded with Au at various ratios (Fig. 5a–f), the as-prepared samples exhibit hollow microsphere morphologies with rough surfaces. In addition, clear gaps are observed between the nanosheets on the microsphere surfaces, indicating their

**Fig. 4** EDS maps of 2 wt.% Au-loaded ZnFe<sub>2</sub>O<sub>4</sub>**Fig. 5** SEM and TEM images of the Au-loaded ZnFe<sub>2</sub>O<sub>4</sub> samples: **a–f** SEM images of pure ZnFe<sub>2</sub>O<sub>4</sub>, 1 wt.% Au-ZnFe<sub>2</sub>O<sub>4</sub>, 2 wt.% Au-ZnFe<sub>2</sub>O<sub>4</sub>, 3 wt.% Au-ZnFe<sub>2</sub>O<sub>4</sub>, and 4 wt.% Au-ZnFe<sub>2</sub>O<sub>4</sub>; **g–h** TEM images of 2 wt.% Au-ZnFe<sub>2</sub>O<sub>4</sub>

porous and loose characteristics. This porous structure may effectively adsorb gas molecules and facilitate their diffusion, leading to excellent gas-sensing performance. As the level of Au doping increases, no significant changes in the sizes or overall hollow structures of the microspheres are observed. Figure 5g, h show the TEM images of 2 wt.% Au-ZnFe<sub>2</sub>O<sub>4</sub>. The sharp contrast between the dark edges and white gaps in the image further confirms the morphology as a surface-roughened hollow microsphere structure, with a corresponding diameter of approximately 1.2  $\mu\text{m}$ .

XPS was performed to investigate the surface chemical compositions and valence states of the 2 wt.% Au-loaded ZnFe<sub>2</sub>O<sub>4</sub> hollow microsphere samples; the results are shown in Fig. 6. In Fig. 6a, the two Zn 2p peaks at 1044.53 and 1021.46 eV are assigned to Zn 2p<sub>1/2</sub> and Zn 2p<sub>3/2</sub>, respectively, indicating that the valence state of Zn in the sample is +2 [50]. In Fig. 6b, the peaks at 713.33 and 710.83 eV

may be ascribed to Fe 2p<sub>3/2</sub> at the tetrahedral (A-site) and octahedral (B-site) sites of the ZnFe<sub>2</sub>O<sub>4</sub> spinel structure, respectively. The peak at 724.86 eV may be attributed to Fe 2p<sub>1/2</sub>, whereas the peaks at 732.69 and 719.24 eV represent the satellite peaks of Fe 2p, indicating that the valence state of Fe in the sample is +3 [29]. In Fig. 6c, the O 1s spectrum displays three peaks at 532.72, 530.92, and 529.93 eV, corresponding to the hydroxyl, surface-adsorbed, and lattice oxygen in the sample, respectively [28]. Based on XPS peak area measurements, the respective relative proportions of these oxygen species are 9.8, 28.8, and 61.4%, and surface-adsorbed oxygen acts favorably to improve the gas-sensing performance of sensitive materials [51]. Based on the Au 4f spectrum in Fig. 6d, the peaks at 92.21 and 88.42 eV are respectively assigned to Zn 3p<sub>1/2</sub> and Zn 3p<sub>3/2</sub> of Zn<sup>2+</sup>. Additionally, the peaks at 87.83 and 83.62 eV represent Au 4f<sub>5/2</sub> and Au 4f<sub>7/2</sub>, respectively, and thus, the valence state of

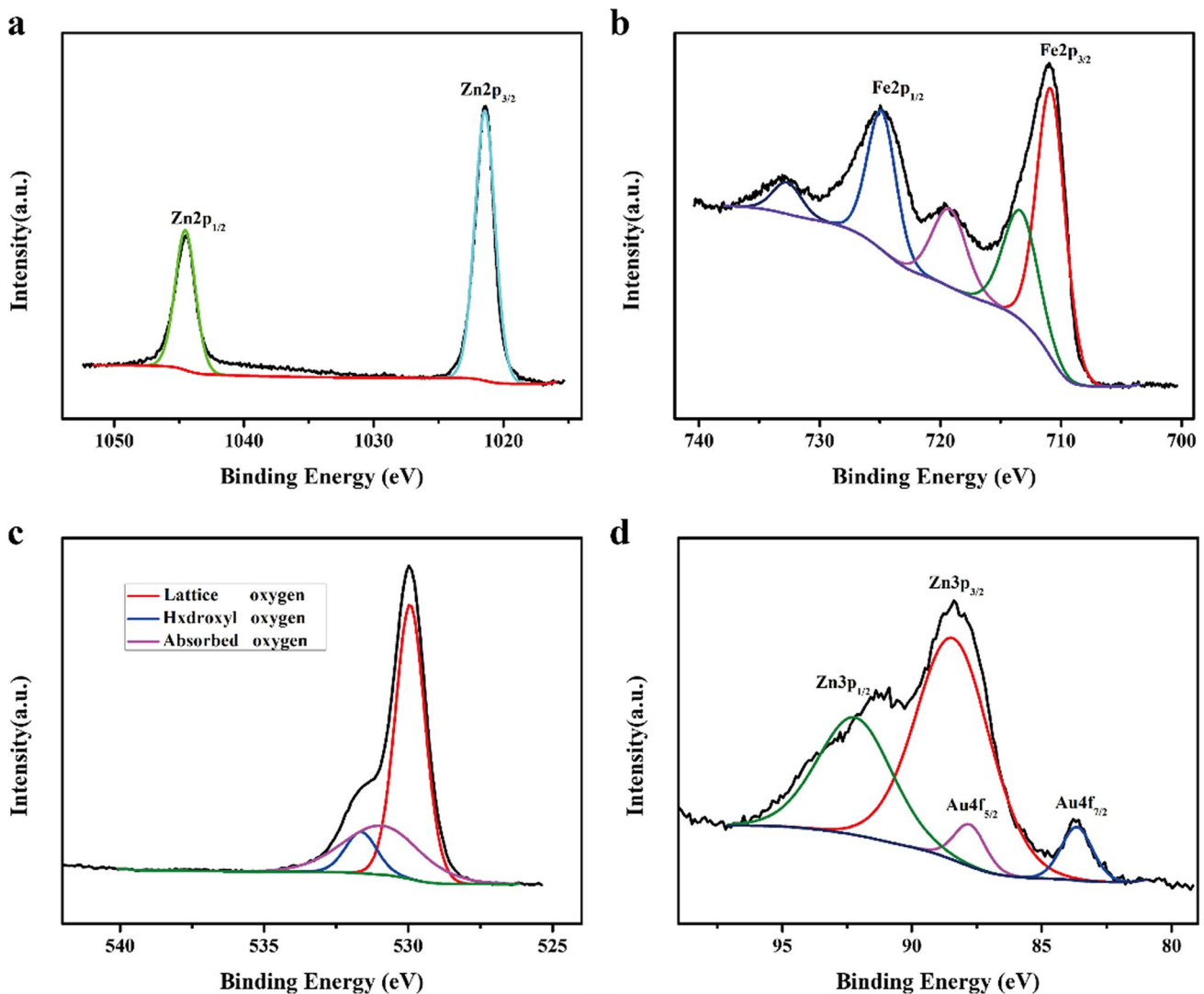
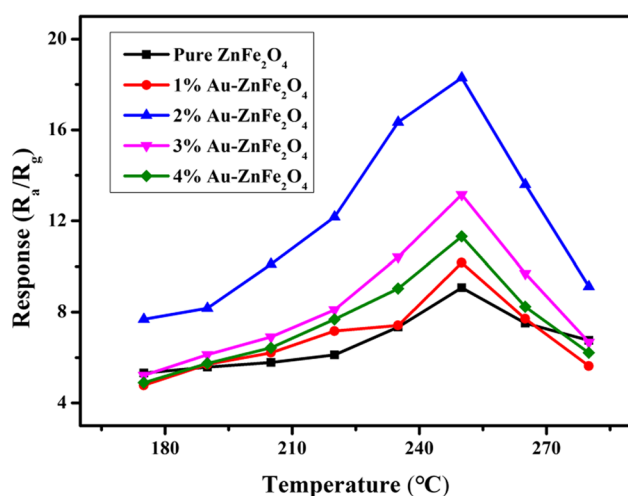


Fig. 6 XPS profiles of 2 wt.% Au-loaded ZnFe<sub>2</sub>O<sub>4</sub>: **a** Zn 2p; **b** Fe 2p; **c** O 1s; and **d** Au 4f

Au in the sample is +1 [52]. The results of XPS, as shown in Fig. 6, are consistent with those of XRD and EDS, further confirming the successful preparation of the Au-loaded  $\text{ZnFe}_2\text{O}_4$  hollow microspheres.

### Gas-sensing properties

The performance of a gas sensor strongly depends on its operating temperature. Figure 7 shows the evaluated sensitivities to 1 ppm of 2-CEES for gas sensors based on Au-loaded  $\text{ZnFe}_2\text{O}_4$  hollow microspheres with different Au loading ratios, operating within the temperature range of 175–280 °C. The responses of the gas sensors to 2-CEES increase and then decrease with an increase in the working



**Fig. 7** Response curves of the  $\text{ZnFe}_2\text{O}_4$  sensors with different Au loading ratios toward 1 ppm of 2-CEES at various working temperatures

temperature, indicating the presence of optimal operating temperatures. This may be explained by the enhancement in target gas diffusion and the increase in the amount of surface-adhered  $\text{O}^-$  on the surface of the sensitive material as the temperature is gradually increased, leading to improved sensitivity. However, as the temperature continues to increase, the diffusion of the target gas gradually becomes saturated. Consequently, the desorption of the target gas plays a dominant role, thereby reducing the sensitivity [26]. In this study, the optimal working temperature of the as-prepared gas sensors is 250 °C. Based on the gas-sensing performances of the Au-loaded  $\text{ZnFe}_2\text{O}_4$  hollow microspheres with different Au loading ratios, the sensor performance initially improves and then deteriorates with increasing Au loading. The gas sensor based on the 2 wt.% Au-loaded  $\text{ZnFe}_2\text{O}_4$  hollow microspheres exhibits the highest sensitivity, and Fig. 8 shows its response and recovery curves. At the optimal working temperature of 250 °C, the gas sensor based on the 2 wt.% Au-loaded  $\text{ZnFe}_2\text{O}_4$  hollow microspheres reaches a sensitivity toward 1 ppm of 2-CEES of 18.29, which is approximately double that of the undoped sensor (9.07). The corresponding response/recovery times also decrease from 18/546 to 12/133 s, respectively, suggesting that Au loading on  $\text{ZnFe}_2\text{O}_4$  may improve the gas-sensing performance. This improvement is mainly attributed to the effect of electronic and chemical sensitization by Au loading [53].

Figure 9a shows the sensing performance of the gas sensor based on the 2 wt.% Au-loaded  $\text{ZnFe}_2\text{O}_4$  hollow microspheres toward 2-CEES within the concentration range of 0.1–3.5 ppm at the optimal working temperature of 250 °C. With an increase in the concentration of 2-CEES, the sensor's sensitivity is enhanced. The sensitivity may still reach 3.56 at a 2-CEES concentration as low as 0.1 ppm,

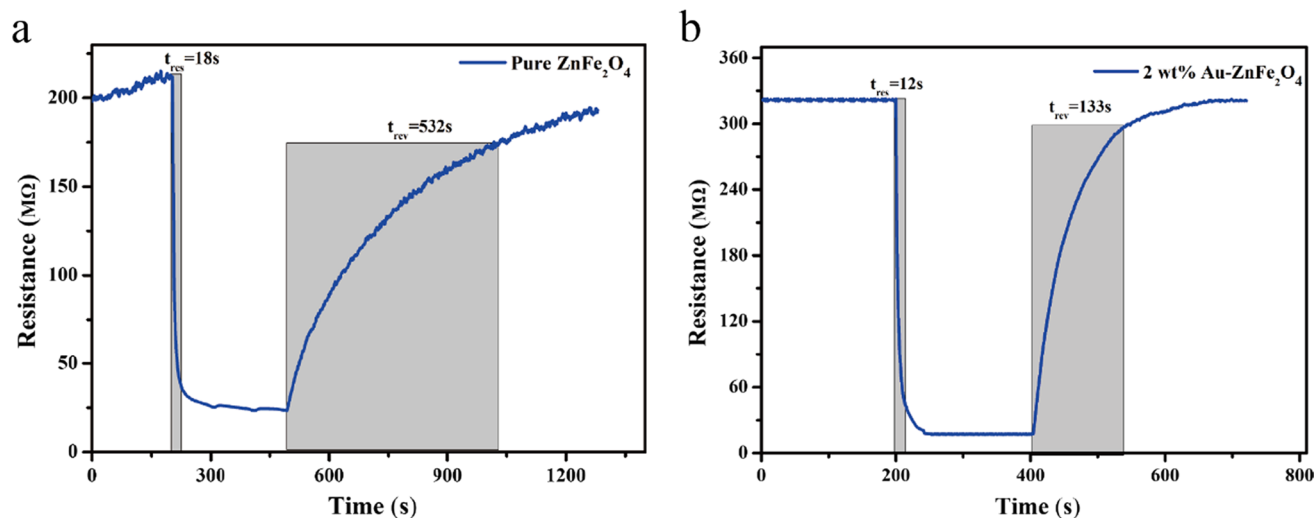


**Fig. 8** Response and recovery curves: Sensors based on **a** pure  $\text{ZnFe}_2\text{O}_4$  and **b** 2 wt.% Au- $\text{ZnFe}_2\text{O}_4$  at 250 °C under 1 ppm of 2-CEES

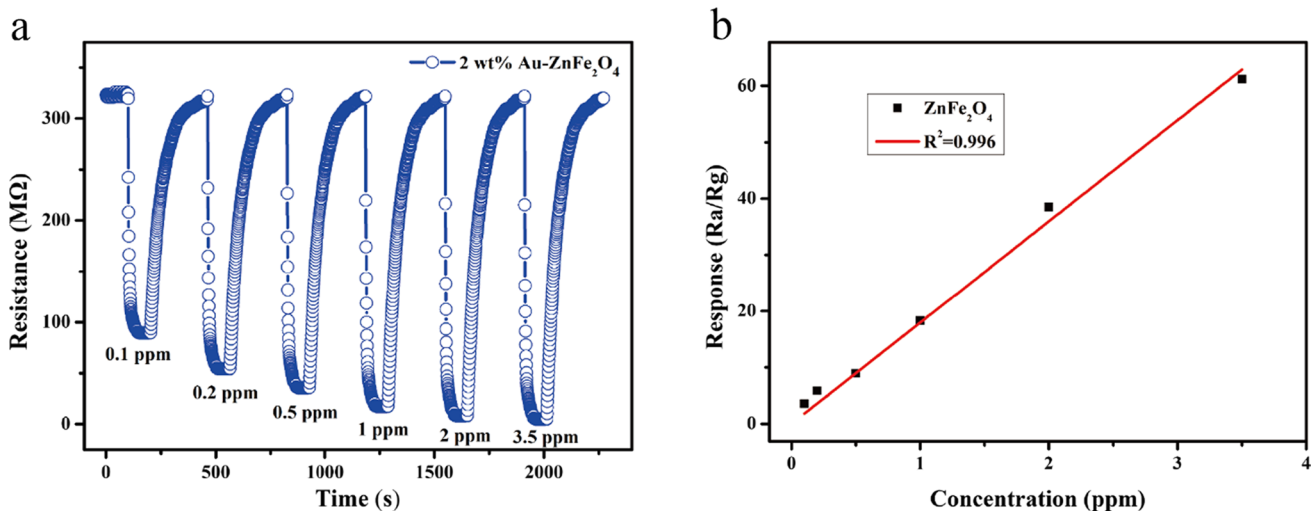


**Fig. 9** Response sensitivity of the sensor based on the 2 wt.% Au-loaded ZnFe<sub>2</sub>O<sub>4</sub> hollow microspheres toward 2-CEES within the concentration range of 0.1–3.5 ppm at the optimal working temperature of 250 °C: **a** Response-recovery curves and **b** linear fitting plot

suggesting that the detection limit of the as-prepared sensor is < 0.1 ppm. As shown in Fig. 9b, the sensor exhibits good linearity within the 2-CEES concentration range of 0.1–3.5 ppm, and the linear correlation coefficient is 0.996, which is highly favorable for the quantitative application of the sensor.

To verify the selectivity of the 2 wt.% Au-loaded ZnFe<sub>2</sub>O<sub>4</sub> hollow microsphere-based gas sensor, it was evaluated for its sensitivities toward 1 ppm of seven different volatile organic gases at the optimal working temperature of 250 °C (Fig. 10a). The sensor exhibits the highest sensitivity towards 2-CEES (18.29) compared to those towards methanol (1.52), ethanol (2.96), acetone (2.64), toluene (1.83),

benzene (1.62), dichloromethane (1.71), and trichloromethane (1.73), indicating the good selectivity of the as-prepared sensor based on the 2 wt.% Au-loaded ZnFe<sub>2</sub>O<sub>4</sub> hollow microspheres towards 2-CEES. At the operating temperature of 250 °C, the gas sensitivities toward 1 ppm of 2-CEES at humidity levels ranging from 20 to 90% were evaluated. As shown in Fig. 10b, the sensitivity of the sensor decreases with increasing humidity. The sensitivity is reduced by approximately 50% at a humidity of 90%, which may be attributed to the competitive adsorption of H<sub>2</sub>O vapor [23].

At a working temperature of 250 °C, continuous response and recovery studies were performed using 1 ppm of 2-CEES. As shown in Fig. 11a, the response and recovery

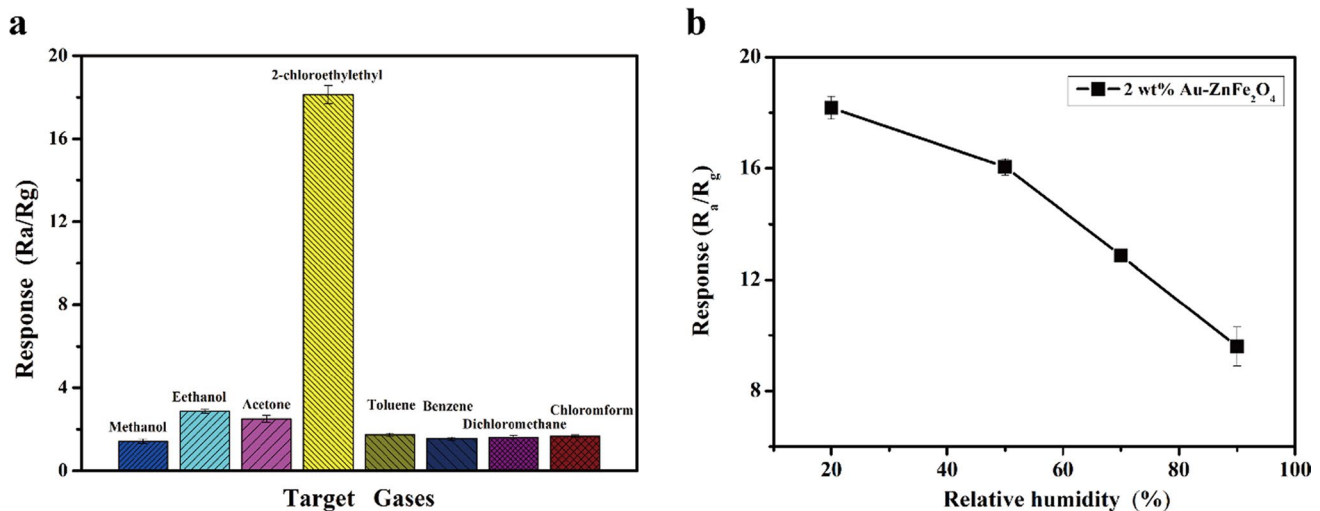


**Fig. 10** **a** Responses of the 2 wt.% Au-loaded ZnFe<sub>2</sub>O<sub>4</sub> hollow microsphere-based sensor to 1 ppm of different gases at 250 °C. **b** Responses of the 2 wt.% Au-loaded ZnFe<sub>2</sub>O<sub>4</sub> hollow microsphere-based sensor to 1 ppm of 2-CEES at different humidities

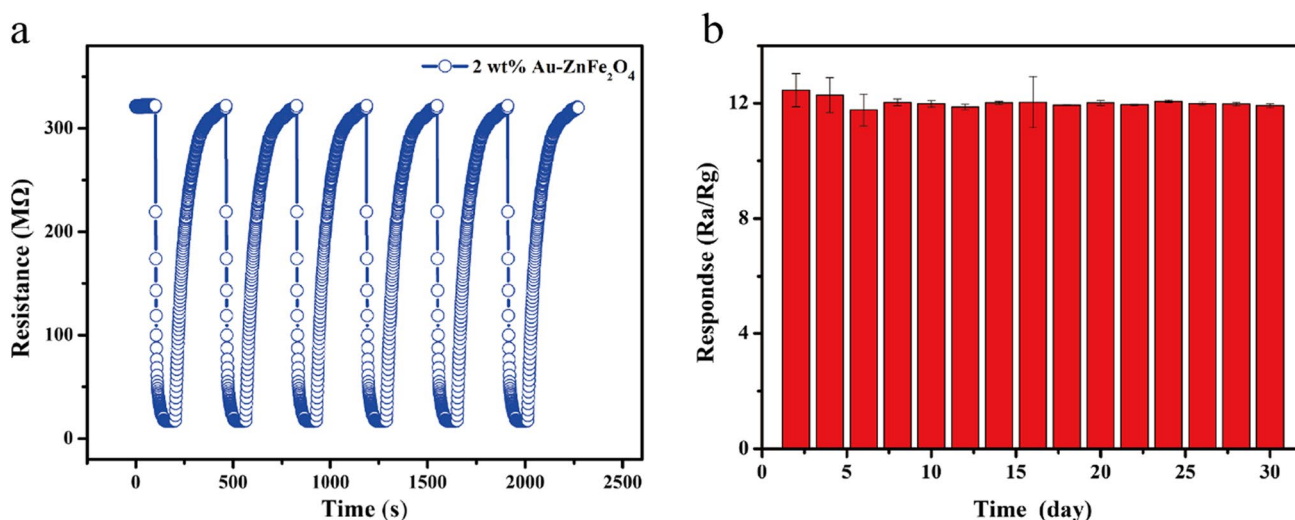


**Fig. 11** **a** Response and recovery curves of the sensor at 250 °C under 1 ppm of 2-CEES in the repeatability study. **b** Sensitivity of the sensor over 30 d of continuous use

curves are consistent, indicating that the sensor exhibits good repeatability. Additionally, the sensitivity of the sensor was monitored over 30 d. As depicted in Fig. 11b, the sensitivity remains relatively stable over the entire period, indicating the good long-term stability and suitability of the sensor for use in continuous monitoring applications.

### Mechanistic analysis

ZnFe<sub>2</sub>O<sub>4</sub> is a typical n-type semiconductor material. Therefore, the gas-sensing mechanism of the ZnFe<sub>2</sub>O<sub>4</sub>-based gas sensor for 2-CEES is primarily attributed to the interactions between 2-CEES and the surface-adsorbed oxygen of the ZnFe<sub>2</sub>O<sub>4</sub> sensing material. These interactions result in a change in the surface electrical resistance of the material, and the corresponding gas-sensing mechanism is illustrated in Fig. 12.

In ambient air, O<sub>2</sub> molecules are adsorbed on the surface of the sensing material and electrons may be extracted from the conduction band, resulting in the formation of more active adsorbed O species (O<sub>2</sub><sup>-</sup>, O<sup>-</sup> and O<sup>2-</sup>) [54, 55]. This may result in the formation of an electron-depleted layer on the surface of the material, thereby enhancing its electrical resistance. At temperatures of < 150 °C, the adsorbed O mainly occurs as O<sub>2</sub><sup>-</sup>, as previously reported [56], and the adsorbed O mainly occurs as O<sup>-</sup> in the temperature range of 150–400 °C. At a temperature of > 400 °C, the adsorbed O mainly occurs as O<sup>2-</sup>, and the reaction is expressed as follows:

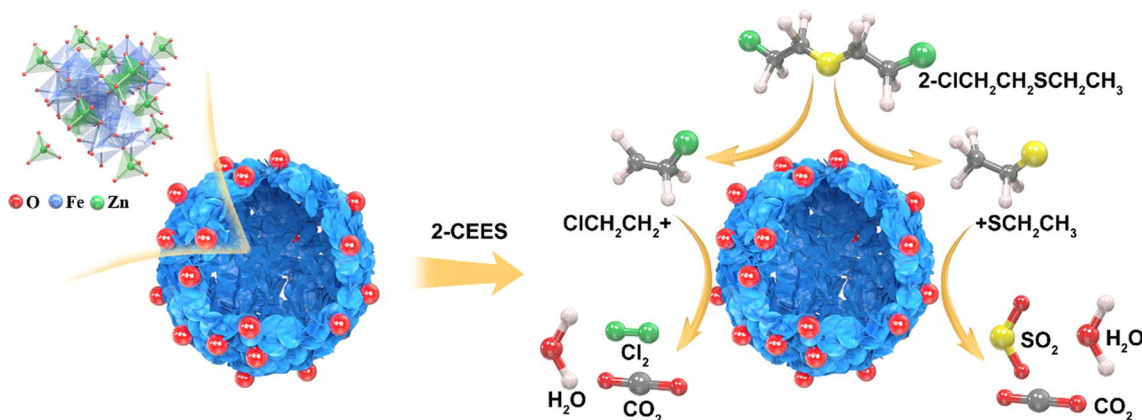
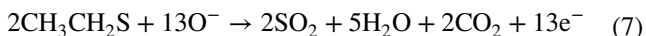
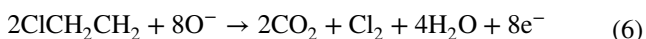
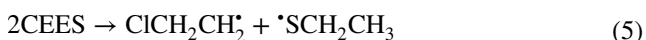


**Fig. 12** Gas-sensing mechanism of the ZnFe<sub>2</sub>O<sub>4</sub> hollow microsphere-based gas sensor for 2-CEES





When the ZnFe<sub>2</sub>O<sub>4</sub> sensor is exposed to the 2-CEES atmosphere, 2-CEES is initially decomposed into two free radicals [17], i.e., ClCH<sub>2</sub>CH<sub>2</sub><sup>•</sup> and <sup>•</sup>SCH<sub>2</sub>CH<sub>3</sub>, which are adsorbed at Lewis acid sites via the Cl and S groups, leading to the surface adsorption of the material. These free radicals may interact with the O<sup>-</sup> adsorbed on the material surface, following which the electrons captured by O<sup>-</sup> may be released back to the conduction band. The thickness of the electron-depleted layer on the material surface decreases, resulting in a reduction in electrical resistance. This reaction can be expressed as follows:



The high gas sensitivity response of the Au-loaded ZnFe<sub>2</sub>O<sub>4</sub> microsphere-based gas sensor to 2-CEES can be attributed to the following four points: First, due to the difference between Zn<sup>2+</sup> and Fe<sup>3+</sup> (such as ionic radius, electronegativity, etc.), ZnFe<sub>2</sub>O<sub>4</sub> with a narrow bandgap width (about 2.1 eV) is more susceptible to heat excitation and produces more electrons, and the oxygen in the air is also easier to capture electrons from the conduction band, producing more adsorbed oxygen, thereby improving the sensitivity. Second, the hollow structure of the ZnFe<sub>2</sub>O<sub>4</sub> microspheres composed of nanosheets is rough and porous, which can provide more active sites and gas adsorption/desorption channels. Again, the Au-modified ZnFe<sub>2</sub>O<sub>4</sub> material has the ability to adsorb and crack oxygen more efficiently, so that the width of the depletion layer on the surface of the material increases, resulting in a decrease in the conductivity of the sensitive material, and as can be seen from Fig. 8, the matrix resistance of the 2 wt% ZnFe<sub>2</sub>O<sub>4</sub> material is significantly higher than that of the undoped ZnFe<sub>2</sub>O<sub>4</sub>. In addition, Au can be used as a catalyst to cleave part of 2-CEES into many more reactive groups, which are more likely to react with oxygen adsorbed on the surface of the material, thereby catalyzing chemical reactions between gases. That is, the electron sensitization and chemical sensitization effects of precious metals, therefore, their response value and response recovery speed have been greatly improved. Finally, based on the high affinity of Au-S, it may be the main reason for its increased selectivity for 2-CEES.

## Conclusions

Au-loaded ZnFe<sub>2</sub>O<sub>4</sub> hollow microspheres with different Au loading ratios were successfully synthesized through a solvothermal method. The chemical compositions and morphological characteristics were analyzed using XRD, EDS, SEM, TEM, and XPS. The sensor based on the as-prepared 2wt% Au-loaded ZnFe<sub>2</sub>O<sub>4</sub> microspheres displayed excellent gas-sensing performance towards the mustard gas simulant 2-CEES. At the optimal temperature of 250 °C, the sensor exhibited a high sensitivity of 18.29 toward 1 ppm of 2-CEES, and the respective response and recovery times were 12 and 133 s. Additionally, the sensor displayed a sensitivity of 3.56 toward concentrations of 2-CEES as low as 0.1 ppm and good selectivity in the presence of methanol, ethanol, acetone, benzene, toluene, dichloromethane, and trichloromethane. The sensor exhibited good repeatability over multiple consecutive response and recovery cycles, and minimal sensitivity fluctuations were observed over a continuous monitoring period of 30 d, indicating that the sensor demonstrated excellent long-term stability. The sensor also exhibited good linearity in the 2-CEES concentration range of 0.1–3.5 ppm. The Au-loaded ZnFe<sub>2</sub>O<sub>4</sub>-based sensor has considerable potential for detecting toxic chemical agents and their simulants.

**Author contributions** Junchao Yang: conceptualization, data curation, investigation, visualization, writing—original draw. Molin Qin: investigation, supervision. Yong Pan: data curation. Liu Yang: data curation, resources. Jianan Wei: a curation, resources. Cancan Yan: data curation. Genwei Zhang: writing—review & editing. Shuya Cao: conceptualization, funding acquisition, supervision. Qibin Huang: conceptualization, funding acquisition, supervision, writing and editing.

**Data availability** Data available on request from the authors.

## Declarations

**Conflict of interest** There are no conflicts to declare.

**Open Access** This article is licensed under a Creative Commons Attribution 4.0 International License, which permits use, sharing, adaptation, distribution and reproduction in any medium or format, as long as you give appropriate credit to the original author(s) and the source, provide a link to the Creative Commons licence, and indicate if changes were made. The images or other third party material in this article are included in the article's Creative Commons licence, unless indicated otherwise in a credit line to the material. If material is not included in the article's Creative Commons licence and your intended use is not permitted by statutory regulation or exceeds the permitted use, you will need to obtain permission directly from the copyright holder. To view a copy of this licence, visit <http://creativecommons.org/licenses/by/4.0/>.

## References

- J.H. Lee, H. Jung, R. Yoo et al., Real-time selective detection of 2-chloroethyl ethyl sulfide (2-CEES) using an Al-doped ZnO quantum dot sensor coupled with a packed column for gas chromatography. *Sens. Actuators, B Chem.* **284**, 444–450 (2019)
- R.M. Fisher, N. Le-Minh, J.P. Alvarez-Gaitan et al., Emissions of volatile sulfur compounds (VSCs) throughout wastewater biosolids processing. *The Science of The Total Environment* **616–617**, 622–631 (2018)
- W.-Q. Meng, A.C. Sedgwick, N. Kwon et al., Fluorescent probes for the detection of chemical warfare agents. *Chem. Soc. Rev.* **52**(2), 61–662 (2023)
- Y. Bai, S. Chen, H. Wang et al., Chemical warfare agents decontamination via air microplasma excited by a triboelectric nanogenerator. *Nano Energy* **95**, 106992 (2022)
- D. Barreca, C. Maccato, A. Gasparotto, Metal oxide nanosystems as chemoresistive gas sensors for chemical warfare agents: a focused review. *Adv. Mater. Interfaces* **9**(14), 2102525–2102551 (2022)
- H. Bu, G. Carvalho, Z. Yuan et al., Biotrickling filter for the removal of volatile sulfur compounds from sewers: a review. *Chemosphere (Oxford)* **277**, 130333–130333 (2021)
- S. Chauhan, S. Chauhan, R. D’Cruz et al., Chemical warfare agents. *Environ. Toxicol. Pharmacol.* **26**(2), 113–122 (2008)
- M. Lafuente, D. Sanz, M. Urbiztondo et al., Gas phase detection of chemical warfare agents CWAs with portable Raman. *J. Hazard. Mater.* **384**, 121279–121279 (2020)
- P. Fehlen, G. Thomas, F. Gonzalez-Posada et al., Gas sensing of organophosphorous compounds with III–V semiconductor plasmonics. *Sens. Actuators, B Chem.* **376**, 132987 (2023)
- T.G. Grissom, A.M. Plonka, C.H. Sharp et al., Metal-organic framework- and polyoxometalate-based sorbents for the uptake and destruction of chemical warfare agents. *ACS Appl. Mater. Interfaces* **12**(13), 14641–14661 (2020)
- J.I. Kim, K.H. Cho, J.H. Lee, et al. Compact, wavelength-selectable, energy-ratio variable Nd:YAG laser at mid-ultraviolet for chemical warfare agent detection[J]. *Curr. Opt. Photon.*, 3(3):243–247 (2019)
- J.-M. Melkonian, J. Armougom, M. Raybaut et al., Long-wave infrared multi-wavelength optical source for standoff detection of chemical warfare agents. *Appl. Opt.* (2004) **59**(35), 11156–11166 (2020)
- Z. Lin, W. Bao-ying, L. Wei-we et al., Rapidly detection of chemical warfare agent simulants by surface enhanced raman spectroscopy. *Guang Pu Xue Yu Guang Pu Fen Xi* **42**(1), 110–114 (2022)
- A. Ahrens, M. Allers, H. Bock et al., Detection of chemical warfare agents with a miniaturized high-performance drift tube ion mobility spectrometer using high-energetic photons for ionization. *Anal. Chem. (Washington)* **94**(44), 15440–15447 (2022)
- L. Zhang, M.-Y. Ma, B.-Q. Li et al., Rapid detection of chemical warfare agent simulants using gold nanoparticles substrate-assisted enhanced low temperature plasma-mass spectrometry. *Fēnxī huàxué* **48**(10), 1416–1421 (2020)
- M. Grabka, Z. Witkiewicz, K. Jasek et al., Acoustic wave sensors for detection of blister chemical warfare agents and their simulants. *Sensors (Basel, Switzerland)*. **22**(15), 5607 (2022)
- J. Yang, L. Yang, S. Cao et al., High-performance metal-oxide gas sensors based on hierarchical core-shell ZnFe<sub>2</sub>O<sub>4</sub> microspheres for detecting 2-chloroethyl ethyl sulfide. *Anal. Methods* **15**(25), 3084–3091 (2023)
- L.A. Patil, V.V. Deo, M.D. Shinde et al., Improved 2-CEES sensing performance of spray pyrolyzed Ru-CdSnO<sub>3</sub> nanostructured thin films. *Sens. Actuators, B Chem.* **191**, 130–136 (2014)
- Z. Witkiewicz, K. Jasek, M. Grabka, Semiconductor gas sensors for detecting chemical warfare agents and their simulants. *Sensors (Basel, Switzerland)*. **23**(6), 3272 (2023)
- A. Dey, Semiconductor metal oxide gas sensors: a review. *Mater. Sci. Eng. B* **229**, 206–217 (2018)
- A. Mirzaei, S.G. Leonardi, G. Neri, Detection of hazardous volatile organic compounds (VOCs) by metal oxide nanostructures-based gas sensors: a review. *Ceram. Int.* **42**(14), 15119–15141 (2016)
- N. Barsan, D. Koziej, U. Weimar, Metal oxide-based gas sensor research: how to? *Sens. Actuators, B Chem.* **121**(1), 18–35 (2007)
- Q. Zheng, T. Wang, B. Li et al., Crosslinked WO<sub>3</sub> nanonet for rapid detection of sulfur mustard gas simulant: mechanism insights and sensing application. *Sens. Actuators, B Chem.* **385**, 133704 (2023)
- R. Yoo, D. Li, H.J. Rim et al., High sensitivity in Al-doped ZnO nanoparticles for detection of acetaldehyde. *Sens. Actuators, B Chem.* **266**, 883–888 (2018)
- L.A. Patil, V.V. Deo, M.D. Shinde et al., Ultrasonically sprayed nanostructured perovskite-type CdSnO<sub>3</sub> thin films for sensing of CWA simulants. *IEEE Sens. J.* **14**(9), 3014–3020 (2014)
- B. Li, X. Ma, Y. Xin et al., In situ construction of hierarchical Fe<sub>2</sub>O<sub>3</sub> nanotube arrays for real-time detection and degradation of 2-CEES gas. *Sens. Actuators, B Chem.* **383**, 133590 (2023)
- K. Wu, J. Li, C. Zhang, Zinc ferrite based gas sensors: A review. *Ceram. Int.* **45**(9), 11143–11157 (2019)
- B. Li, X. Zhang, L. Huo et al., Controllable construction of ZnFe<sub>2</sub>O<sub>4</sub>-based micro-nano heterostructure for the rapid detection and degradation of VOCs. *J. Hazard. Mater.* **435**, 129005–129005 (2022)
- X. Zhou, B. Wang, H. Sun et al., Template-free synthesis of hierarchical ZnFe<sub>2</sub>O<sub>4</sub> yolk-shell microspheres for high-sensitivity acetone sensors. *Nanoscale* **8**(10), 5446–5453 (2016)
- X. Li, C. Han, D. Lu et al., Highly electron-depleted ZnO/ZnFe<sub>2</sub>O<sub>4</sub>/Au hollow meshes as an advanced material for gas sensing application. *Sens. Actuators, B Chem.* **297**, 126769 (2019)
- K. Li, Y. Luo, L. Gao et al., Au-decorated ZnFe<sub>2</sub>O<sub>4</sub> yolk-shell spheres for trace sensing of chlorobenzene. *ACS Appl. Mater. Interfaces* **12**(14), 16792–16804 (2020)
- S.-K. Shen, X.-L. Cui, C.-Y. Guo et al., Sensing mechanism of Ag/ $\alpha$ -MoO<sub>3</sub> nanobelts for H<sub>2</sub>S gas sensor. *Rare Met.* **40**(6), 1545–1553 (2021)
- M.S. Barbosa, P.H. Suman, J.J. Kim et al., Investigation of electronic and chemical sensitization effects promoted by Pt and Pd nanoparticles on single-crystalline SnO nanobelt-based gas sensors. *Sens. Actuators, B Chem.* **301**, 127055 (2019)
- J. Wang, Q. Zhou, Z. Lu et al., Gas sensing performances and mechanism at atomic level of Au-MoS<sub>2</sub> microspheres. *Appl. Surf. Sci.* **490**, 124–136 (2019)
- Z. Zhao, D. Jiang, Y. Xue et al., Synthesis and characterization of AuNPs-modified Fe<sub>2</sub>O<sub>3</sub>/ZnFe<sub>2</sub>O<sub>4</sub> heterostructures for highly sensitive 1-butanol detection. *J. Mater. Sci.* **56**(30), 16963–16975 (2021)
- Z. Wang, Z. Tian, D. Han et al., Highly sensitive and selective ethanol sensor fabricated with in-doped 3DOM ZnO. *ACS Appl. Mater. Interfaces* **8**(8), 5466–5474 (2016)
- S. Bai, S. Chen, Y. Zhao et al., Gas sensing properties of Cd-doped ZnO nanofibers synthesized by the electrospinning method. *Journal of Materials Chemistry. A, Materials for energy and sustainability* **2**(39), 16697–16706 (2014)
- H. Gao, Q. Yu, S. Zhang et al., Nanosheet-assembled NiO microspheres modified by Sn<sup>2+</sup> ions isovalent interstitial doping for xylene gas sensors. *Sens. Actuators, B Chem.* **269**, 210–222 (2018)

39. D.R. Miller, S.A. Akbar, P.A. Morris, Nanoscale metal oxide-based heterojunctions for gas sensing: a review. *Sens. Actuators, B Chem.* **204**, 250–272 (2014)
40. D. Zappa, V. Galstyan, N. Kaur et al., “Metal oxide -based heterostructures for gas sensors”- a review. *Anal. Chim. Acta* **1039**, 1–23 (2018)
41. J.M. Walker, S.A. Akbar, P.A. Morris, Synergistic effects in gas sensing semiconducting oxide nano-heterostructures: a review. *Sens. Actuators, B Chem.* **286**, 624–640 (2019)
42. H. Wang, J. Ma, J. Zhang et al., Gas sensing materials roadmap. *J. Phys. Condens. Matter* **33**(30), abf477 (2021)
43. H. Ji, W. Zeng, Y. Li, Gas sensing mechanisms of metal oxide semiconductors: a focus review. *Nanoscale* **11**(47), 22664–22684 (2019)
44. G. Korotcenkov, B.K. Cho, Metal oxide composites in conductometric gas sensors: achievements and challenges. *Sens. Actuators, B Chem.* **244**, 182–210 (2017)
45. M.I. Nemifulwi, H.C. Swart, G.H. Mhlongo, Evaluation of the effects of Au addition into ZnFe<sub>2</sub>O<sub>4</sub> nanostructures on acetone detection capabilities. *Mater. Res. Bull.* **142**, 111395 (2021)
46. B. Yang, C. Wang, R. Xiao et al., High sensitivity and fast response sensor based on sputtering Au tuned ZnFe<sub>2</sub>O<sub>4</sub>-SE for low concentration NH<sub>3</sub> detection. *Mater. Chem. Phys.* **239**, 122302 (2020)
47. Y. Yan, P. Nizamidin, G. Turdi et al., Room-temperature H<sub>2</sub>S gas sensor based on Au-doped ZnFe<sub>2</sub>O<sub>4</sub> yolk-shell microspheres. *Anal. Sci.* **33**(8), 945–951 (2017)
48. J.-H. Kim, A. Mirzaei, H.W. Kim et al., Combination of Pd loading and electron beam irradiation for superior hydrogen sensing of electrospun ZnO nanofibers. *Sens. Actuators, B Chem.* **284**, 628–637 (2019)
49. L.A. Patil, V.V. Deo, M.D. Shinde et al., Sensing of 2-chloroethyl sulfide (2-CEES) – a CWA simulant – using pure and platinum doped nanostructured CdSnO<sub>3</sub> thin films prepared from ultrasonic spray pyrolysis technique. *Sens. Actuators, B Chem.* **160**(1), 234–243 (2011)
50. C. Zhang, Q. Wu, B. Zheng et al., Synthesis and acetone gas sensing properties of Ag activated hollow sphere structured ZnFe<sub>2</sub>O<sub>4</sub>. *Ceram. Int.* **44**(17), 20700–20707 (2018)
51. Y. Fan, K. Li, X. Ren et al., A highly selective gas sensor based on the WO<sub>3</sub>/WS<sub>2</sub> van der waals heterojunction for the 2-chloroethyl ethyl sulfide (2-CEES) sensing application. *Journal of Materials Chemistry C* **9**(48), 17496–17503 (2021)
52. M.I. Nemifulwi, H.C. Swart, G.H. Mhlongo, Evaluation of the effects of Au addition into ZnFe<sub>2</sub>O<sub>4</sub> nanostructures on acetone detection capabilities. *Mater. Res. Bull.* **142**, 111395 (2021)
53. M. Lee, M.Y. Kim, J. Kim et al., Conductometric sensor for gaseous sulfur-mustard simulant by gold nanoparticles anchored on ZnO nanosheets prepared via microwave irradiation. *Sens. Actuators, B Chem.* **386**, 133726 (2023)
54. J. Liu, L. Zhang, J. Fan et al., Triethylamine gas sensor based on Pt-functionalized hierarchical ZnO microspheres. *Sens. Actuators, B Chem.* **331**, 129425 (2021)
55. C. Wang, Y. Wang, P. Cheng et al., In-situ generated TiO<sub>2</sub>/α-Fe<sub>2</sub>O<sub>3</sub> heterojunction arrays for batch manufacturing of conductometric acetone gas sensors. *Sens. Actuators, B Chem.* **340**, 129926 (2021)
56. A. Hermawan, B. Zhang, A. Taufik et al., CuO Nanoparticles/Ti<sub>3</sub>C<sub>2</sub>T<sub>x</sub> MXene hybrid nanocomposites for detection of toluene gas. *ACS Appl. Nano Mater.* **3**(5), 4755–4766 (2020)